Petroleum Science 19 (2022) 619–628

Contents lists available at ScienceDirect

Petroleum Science

journal homepage: www.keaipublishing.com/en/journals/petroleum-science

Original Paper

Experimental investigation and correlations for proppant distribution in narrow fractures of deep shale gas reservoirs

Hao Zeng [a], Yan Jin [a], Hai Qu [b, *], Yun-Hu Lu [a]

[a] College of Petroleum Engineering, China University of Petroleum (Beijing), Beijing, 102249, China
[b] College of Petroleum Engineering, Chongqing University of Science and Technology, Chongqing, 401331, China

ARTICLE INFO

Article history:
Received 23 May 2021
Accepted 26 September 2021
Available online 23 October 2021

Edited by Yan-Hua Sun

Keywords:
Proppant transport
Multiphase flow
Hydraulic fracturing
Deep reservoir
Narrow fractures

ABSTRACT

Hydraulic fracturing is a crucial stimulation for the development of deep shale gas reservoirs. A key challenge to the effectiveness of hydraulic fracturing is to place small proppants in complex narrow fractures reasonably. The experiments with varied particle and fluid parameters are carried out in a narrow planar channel to understand particle transport and distribution. The four dimensionless parameters, including the Reynold number, Shields number, density ratio, and particle volume fraction, are introduced to describe the particle transport in narrow fractures. The results indicate that the narrow channel probably induces fluid fingers and small particle aggregation in a highly viscous fluid, leading to particle settlement near the entrance. The low viscous fluid is beneficial to disperse particles further into the fracture, especially in the high-speed fluid velocity. The linear and natural logarithmic laws have relationships with dimensionless parameters accurately. The multiple linear regression method developed two correlation models with four dimensionless parameters to predict the bed equilibrium height and covered area of small particles in narrow fractures. The study provides fundamental insight into understanding small size proppant distribution in deep reservoirs.

1. Introduction

Understanding the fundamental aspects of particle transport is of relevance to comprehensive nature phenomena and engineering applications, such as sand deposition in rivers and lakes (Dominguez Ruben et al., 2020), stream turbine analysis (Li et al., 2020), water reservoir management (Ren et al., 2020), etc. In the petroleum industry, proppant particle transport within fractures created by hydraulic fracturing is crucial in improving shale gas reservoir production, featuring low porosity and permeability (Qu et al., 2020; Zeng et al., 2019). With the development of the deep shale gas reservoirs, a salient feature of such fractures is very narrow due to the high confining stress. Thus, various small-size proppants, such as 40/70 mesh and 70/140 mesh, are widely used to improve particle transport and avoid particle plugging in narrow pathways. A better understanding of the distribution characteristics of small proppants in such wall-bounded narrow fractures is central to predicting particle placement and optimizing engineering design.

Since the proppant bed shape directly affects fracture conductivity, the height and coverage area of the particle bed are two key parameters to evaluate particle transport and deposition in fractures (Miskimins, 2020). Correspondingly, the fluid mixed with particles is pumped into a laboratory-scale, homogeneous channel, and the bed size is measured. Kern et al. (1959) performed the first work in a planar acrylic channel with the sizes of 0.56 m (length) × 0.19 m (height) × 6.35 mm (width). The 20/40 mesh sand mixed with water was pumped into the channel, and the bed grows until the height reaches the equilibrium value. A mathematic equation of the equilibrium height was proposed according to the experimental result. Then, Babcock et al. (1967) constructed a longer channel (2.44 m × 0.3 m × 6 mm) to test the equilibrium fluid velocity and bed buildup rate as the sand bed reaches the equilibrium state. The corresponding correlations were developed to predict particle deposition in both Newtonian and non-Newtonian fluids. Since the experimental particles were large sands, including 8/12, 10/20, and 20/40 mesh, the equations are suitable for predicting the bed shape of large particles. Schols and Visser (1974) extended the work and developed analytical relations to predict the bed shape in a 6.3-mm wide channel, including the height, length, and slope angle. In addition, Novotny

* Corresponding author.
E-mail address: quhai729@163.com (H. Qu).

https://doi.org/10.1016/j.petsci.2021.10.019

(1977) proposed numerical equations considering the fluid leak-off, wall effects, and hindered settling velocity.

Based on the experimental channel (2.44 m × 0.3 m × 8 mm) made in STM-LAB Inc, Patankar et al. (2002) and Wang et al. (2003) developed the implicit power and explicit bi-power correlations. The correlations have calibrated the numerical models and compared them with experimental results in a planar channel (Sahai et al., 2014; Tong and Mohanty, 2016). Patankar et al. (2002) introduced the dimensionless numbers representing the fluid velocity, particle density, and particle size. The particle types have the silica-sand of 10/20 mesh, 20/40 mesh, and 40/50 mesh, heavy carbolite of 16/20 mesh, and light beads of 20/40 mesh. Then, Wang et al. (2003) developed the famous explicit correlations used in the field treatment of hydraulic fracturing by Woodworth and Miskimins (2007). Mack et al. (2014) used a correlation based on the Shields number to evaluate proppant deposition and then proposed to use this equation for hydraulic fracturing design. According to the dimensionless theory, Alotaibi and Miskimins (2018) also obtained a power-law correlation between the bed equilibrium height and fluid velocity to predict 30/70 mesh sand deposition in the planar channel with the sizes of 1.2 m (length) × 0.6 m (height) × 5.8 mm (width). In addition, abundant transport mechanisms in the narrow channel were discussed in detail.

As mentioned above, the previous studies mainly focus on the large particles deposited in a wide fracture, which is typically created in shallow conventional reservoirs. However, few scholars have been able to draw on any systematic research about small particle transport in a narrow wall-bounded fracture for the situation of the deep reservoirs. Also, there are no relevant models to quantitatively predict the bed equilibrium height and coverage area for optimizing the hydraulic fracturing treatment. Thus, the purpose of this investigation is to specifically explore the relationship between small particles and the narrow channel for a better understanding of the transport behaviors in the deep shale reservoir. The article is organized as follows: In Section 2, an experimental system and procedures are introduced. A 3-mm wide channel is assembled. Nine types of natural particles are used to improve compatibility between the laboratory experiment and field application. The four dimensionless parameters are used to analyze the effects of fluid velocity, fluid viscosity, particle density, particle size, and particle volume fraction on particle distribution. In Section 3, sensitivity analysis is investigated. The multiple linear regression method developed two correlation models expressed by four dimensionless numbers to predict the proppant bed's equilibrium height and coverage area.

2. Experimental method

2.1. Experimental system

Fig. 1 represents a schematic diagram of the particle-fluid flow system. A progress cavity pump with a variable frequency driver (VFD) is used to achieve the requirement of the slurry rate. The slurry is pumped into the channel by five holes on the inlet panel to simulate the injection effect of the perforation, and the hole diameter is 9 mm. In the channel without deposited particles, the mean fluid velocities can achieve 0.17, 0.21, 0.42, and 0.5 m/s by VFD. The velocity range is similar to the literature (Qu et al., 2021b; Sahai et al., 2014). Particles are premixed with fluid in a tank, and the maximum volume fraction is 4.2%. Two high-definition cameras record slurry flow and particle bed accumulation in the channel. Moreover, a pressure sensor is installed at the inlet to record liquid pressure. The slurry flows out of the slots discharged through the five holes on the outlet panel to the recycle tank. The inlet and outlet configurations are similar to the channel in the literature (Ba Geri et al., 2018; Fernández et al., 2019; Mack et al., 2014; Qu et al., 2021a). The channel is assembled by two transparent acrylic panels and achieves the sizes of 1.5 m (length) × 0.27 m (height) × 3 mm (width). As the particle bed reaches the equilibrium state that the shape is constant, we stop the test and record the total injected time.

2.2. Fluid and particle

Water and slickwater with low viscosity are used as the fluid to mix with proppant particles. The slickwater as a non-Newton fluid is a typical fracturing fluid and is made up of a chemical agent of polyacrylamide. The water viscosity is 0.001 Pa s, and viscosities of three types of slickwater are 0.003, 0.006, and 0.009 Pa s, respectively. Fig. 2 shows the liquid samples of water and slickwater.

Three types of 40/70 mesh particles, including quartz sand, ceramsite, and garnet, are selected to achieve particle density difference, as shown in Fig. 3(a). Fig. 3(b) and (c) show three types of natural sands and garnets with 10/20 mesh, 20/40 mesh, and 70/140 mesh. Sieves determined the size distributions of 20/40 mesh particles. For other mesh particles, a laser particle size analyzer is used to measure the size distributions. Particle parameters are listed in Table 1. Sphericity is a geometrical form parameter representing the degree to which a particle approximates a perfect sphere, and the equation can be found in the literature (Zheng et al., 2018). The crushing rates of proppant are obtained from suppliers, and the test method can be found in the literature (Zheng et al., 2018). It should be noted that the crushed tests were carried out under the compressive stress of 28 MPa.

2.3. Experimental parameters

Dimensionless parameters are commonly used to develop experimental models based on the Buckingham PI theorem (Zohuri, 2017). It is considered to be very effective when several variables are involved in the particle-fluid flow. According to the theory, some authors have been derived the models from analyzing proppant transport in the horizontal wellbore and complex fracture (Ahmad and Miskimins, 2020; Fjaestad and Tomac, 2019; Li et al., 2018; Mack et al., 2014; Wang et al., 2003). In this work, two dependent variables are the height and coverage area of the particle bed. The independent variables include fluid velocity, fluid viscosity, particle density, particle size, and particle volume fraction. Based on the analysis of particle-fluid flow (Ahmad and Miskimins, 2020; Li et al., 2018; Mack et al., 2014), the dimensionless number of the bed equilibrium height and coverage area can be expressed by Eq. (1).

$$\mathrm{BEH},\ \mathrm{BCA} = f\left(Re_{\mathrm{f}},\ S, \frac{\rho_{\mathrm{p}}}{\rho_{\mathrm{f}}}, C_{\mathrm{p}}\right) \tag{1}$$

where BEH is the percentage of bed equilibrium height expressed by Eq. (2); BCA is the percentage of coverage area expressed by Eq. (3); Re_{f} is the fluid Reynold number; ρ_{f} is the fluid density, kg/m^3; ρ_{p} is the particle density, kg/m^3; S is the Shields number expressed by Eq. (6); C_{p} is the particle volume fraction expressed by Eq. (7).

$$\mathrm{BEH} = \frac{H_{\mathrm{b}}}{H} \times 100\% \tag{2}$$

$$\mathrm{BCA} = \frac{A_{\mathrm{b}}}{A_{\mathrm{c}}} \times 100\% \tag{3}$$

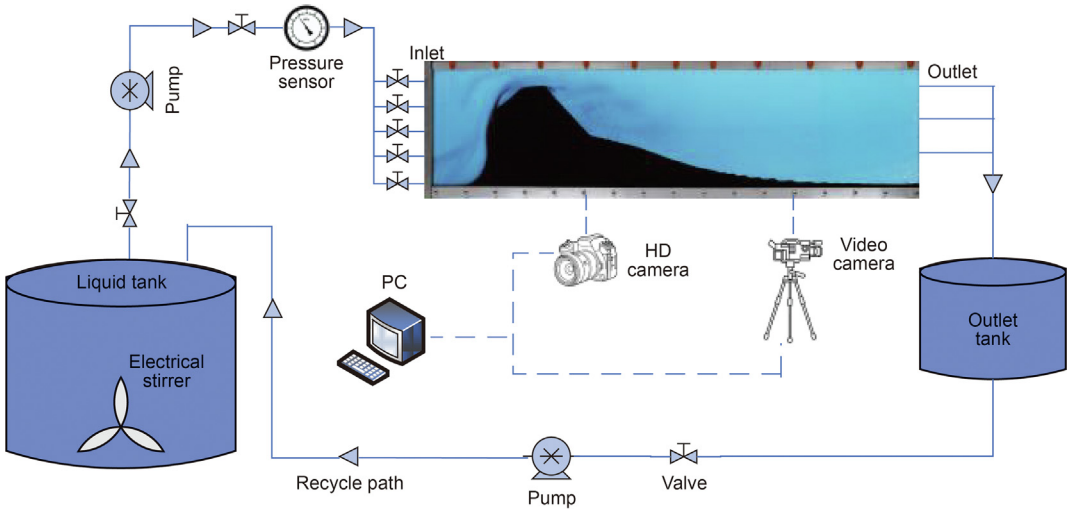

Fig. 1. Schematic of the particle-fluid flow experiment.

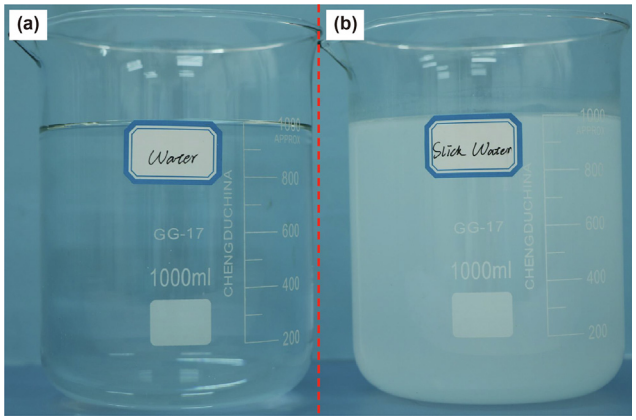

Fig. 2. The liquid samples. (**a**) Water (0.001 Pa s); (**b**) Slickwater (0.009 Pa s).

where H_b is the bed equilibrium height, m; H is the slot height, m.

The Reynold number in the narrow channel can be expressed by Eq. (4) (Tong and Mohanty, 2016).

$$Re_f = \frac{\rho_f v_i D_h}{\mu_f} \tag{4}$$

where v_i is the mean fluid velocity in the slot, m/s; μ_f is the fluid viscosity, Pa s; D_h is the hydraulic diameter of the channel and defined as

$$D_h = \frac{2wh}{w+h} \tag{5}$$

where h is the channel height; w is the channel width.

Shields number is a crucial dimensionless parameter representing the shear stress ratio at the top of the particle bed to the apparent weight of a single particle. Mack et al. (2014) proposed the equation in a narrow rectangular flow slot expressed by Eq. (6). The Shields number can represent the particle diameter.

$$S = \frac{8 v_i \mu_f}{\left(\rho_p - \rho_f\right) g d_p w} \tag{6}$$

where d_p is the average grain diameter d_{50}, m.

The particle volume fraction is a typical dimensionless number, which can be calculated by Eq. (7).

$$C_p = \frac{q_p}{q_p + q_f} \times 100\% \tag{7}$$

where q_p is the particle flow rate, m^3/min; q_f is the fluid flow rate, m^3/min.

3. Results and discussion

3.1. Transport mechanisms

Fig. 4 displays three snapshots of 40/70 mesh garnet transport in slickwater at $v_i = 0.42$ m/s, $\mu_f = 0.006$ Pa s, $C_p = 4.2\%$. The Reynolds number Re_f predicted flow regimes effectively indicates the flow characteristics in a straight narrow slot (Miller et al., 1977). For the flow between parallel plates, the transition from laminar to turbulent flow occurs at a critical value in the range of 2000–3000 (McClure, 2018). The flow is pure laminar as Re_f is less than 2000. According to Eq. (4), the Reynold number is 415 indicating the laminar flow as there are no deposited particles in the slot. With the particle settling, it is observed that the flow region significantly decreases from 60 to 210 s. The decrease of the flow region increases the fluid velocity and changes the slurry flow pattern. Fig. 5(a) shows the bed profiles digitalized by GetData Graph Digitizer, which is a program for digitizing graphs (http://getdata-graph-digitizer.com/). Since the injected flow rate is constant, the fluid velocity would increase from the entrance to the outlet due to the upward inclined bed. In Fig. 5(b), the Reynold number in the top gap increases from 415 to 1692 as the length is equal to 1300 mm. Although the flow pattern is laminar, the slurry flow velocity increases four times from 0.42 to 1.77 m/s.

In the viscous fluid, the suspension particles in the top gap are clearly observed at three moments. Besides, a fluidization layer on the top of the bed and the stationary bed can be found. The three-layer flow pattern is similar to the results (Liu, 2006; Zhang et al.,

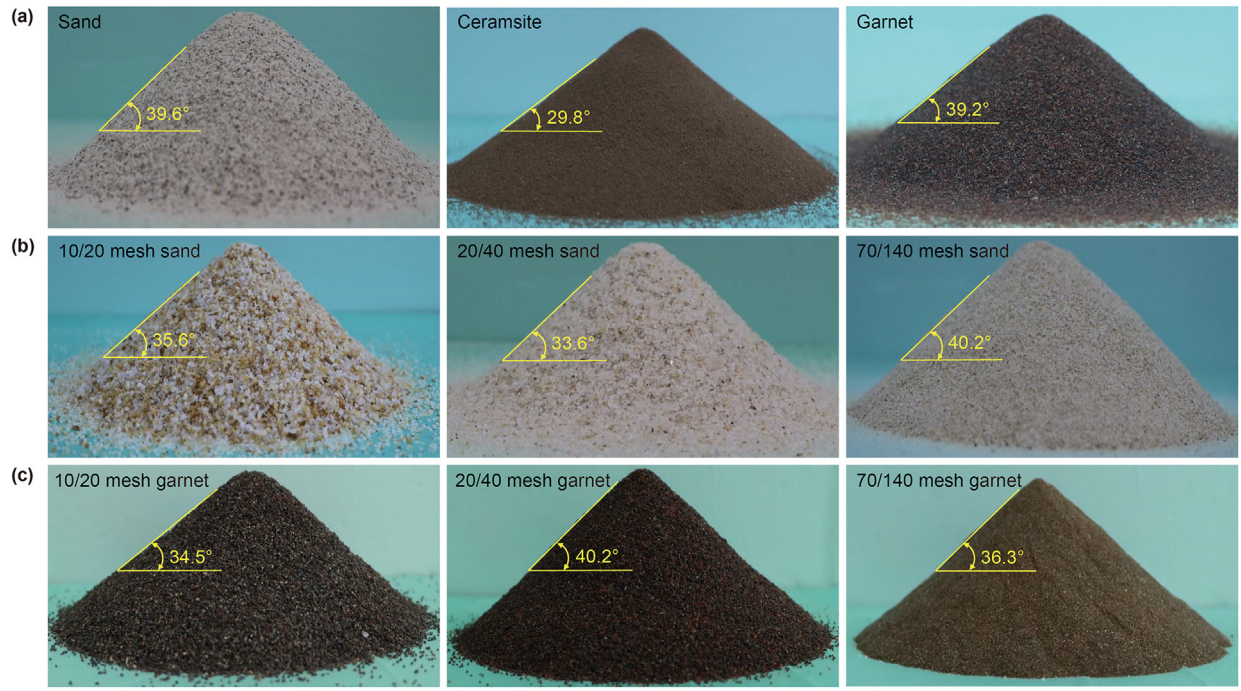

Fig. 3. Particle samples in the experiments. (**a**) 40/70 mesh particles; (**b**) Sand; (**c**) Garnet.

Table 1
Particle parameters used in experiments.

Material	Mesh	Sieve size, mm	Average grain diameter d_{50}, mm	Density ρ_p, kg/m^3	Bulk density ρ_b, kg/m^3	Sphericity	Repose angle θ_r, degree	Crushing rate, %
Quartz sand	10/20	2/0.84	1.410	2650	1792	0.85	35.6	17.2
	20/40	0.84/0.42	0.633	2650	1698	0.82	33.6	15.1
	40/70	0.43/0.106	0.311	2650	1670	0.85	39.6	9.8
	70/140	0.29/0.053	0.155	2650	1645	0.86	40.2	3.1
Ceramsite	40/70	0.44/0.105	0.257	3300	1937	0.90	29.8	3.4
Garnet	10/20	2.2/0.9	1.560	3900	2010	0.81	34.5	13.2
	20/40	0.81/0.42	0.566	3900	2036	0.83	40.2	12.1
	40/70	0.41/0.101	0.242	3900	2056	0.83	39.2	6.7
	70/140	0.29/0.05	0.121	3900	2010	0.81	36.3	2.2

2017). In Fig. 4(a), particle aggregation is clearly observed along the whole channel at the early injected stage, and many aggregated garnets quickly deposit on the bottom along with the channel. During the experiment, some particles are directly suspended into the outlet tank by slickwater as the specific gravity is 3.9. As the bed builds up, an important finding is that fluid fingers appear, and particle aggregation is more prominent in the channel, as shown in Fig. 4(b) and (c). Liu and Sharma (2005) also reported that rough walls induce fluid fingers in a 6-mm wide channel. However, it should be noted that the mechanisms of fluid fingers are different. In the experiment reported by Liu and Sharma (2005), the irregular surfaces could induce an uneven velocity profile in the direction of the fracture height. The wider aperture is beneficial to the slurry flow, while the narrower aperture hinders flow. Thus, the fluid fingers are formed in the natural fracture. For our smooth channel, the probable reason is that the narrow pathway and the decrease of flow gap significantly limit particle dispersion in the width and height directions. Since the flow gap gradually decreases, the high-speed flow could destruct fingers to many particle clusters. Due to the increase in weight, particle aggregation quickly leads to more particle settlement (Fjaestad and Tomac, 2019). In Fig. 4(c), the final particle bed is near the inlet and reaches the equilibrium state with a constant shape. The injected particles directly flow out of the channel and would not deposit in the channel.

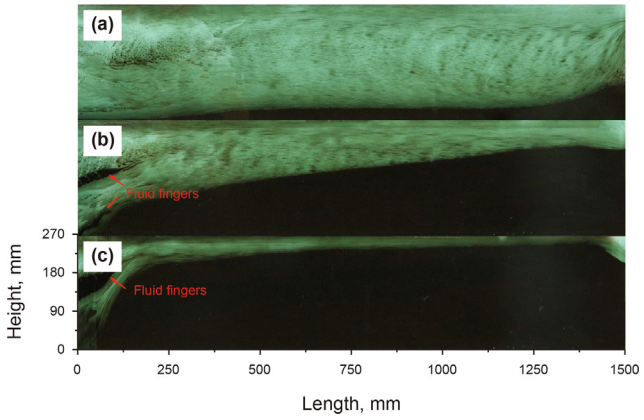

Fig. 4. Snapshoots of particle transport and placements in the narrow channel at three injection times for 40/70 mesh garnet at $v_i = 0.42$ m/s, $\mu_f = 0.006$ Pa s, $C_p = 4.2\%$, front view. (**a**) 60 s; (**b**) 150 s; (**c**) 210 s.

Fig. 6 presents the front view of 40/70 mesh particle beds at the equilibrium state in water at $v_i = 0.42$ m/s, $\mu_f = 0.001$ Pa s, $C_p = 4.2\%$. The three-layer flow pattern is also observed in Fig. 6(a) to 6(c). Since the sand color is light white, it is difficult to capture the

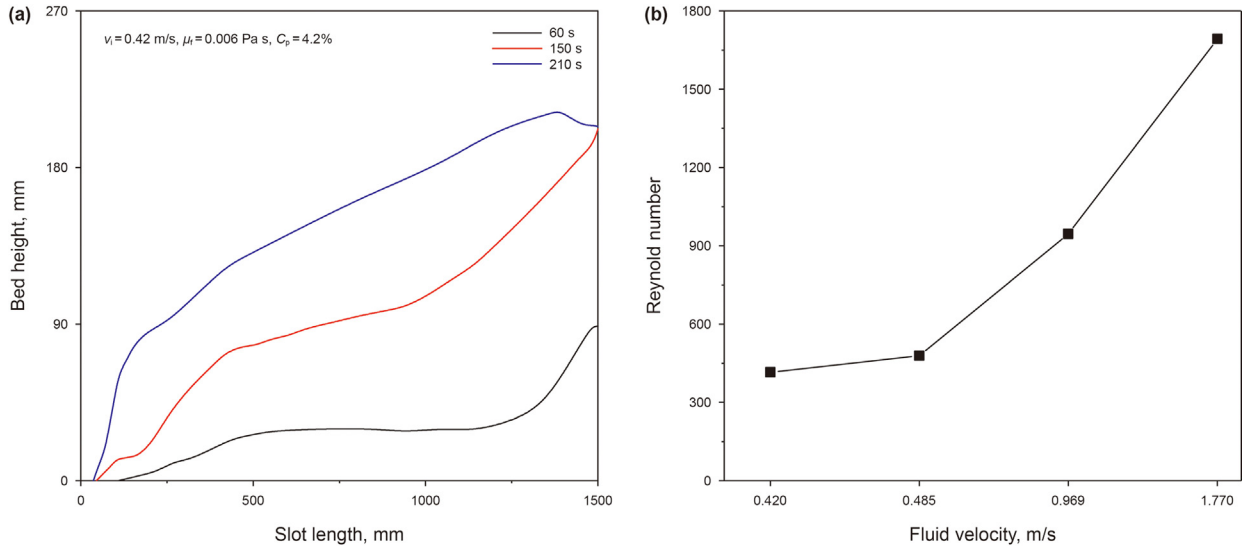

Fig. 5. (**a**) Profiles of particle bed at three moments; (**b**) Reynold numbers and fluid velocities in the top gap at the slot length of 1300 mm.

movement state by the HD camera, especially in the front of the channel. The high-speed fluid flow from the injected holes induces the turbulent flow near the entrance and forms vortexes identical to the literature (Liu, 2006). The violent vortexes could quickly disperse particles after the injection and lift them over the top of the stationary bed. Also, a proppant depleted region is formed between the slot entrance and particle bed. It is also found that the slope angles in the front of the bed are more than the corresponding repose angle in the air. Fig. 7(a) shows that the particle bed profiles at the equilibrium state. With the increase in particle density, a higher bed would be formed near the inlet and the particle bed's coverage area increases. After 750 mm in length, a constant bed height could be found, and the height increases with the increase of the particle density.

In Fig. 7(b), as the density ratio increases from 2.65 to 3.9, the BEH increases from 71.4% to 83.3%, and the BCA increases from 49.9% to 65.2%. Fitting linear trends through the experimental results yields a coefficient of determination, R^2 of 0.97. Fig. 7(c) measures the volumes of injection particles in the channel and outlet tank. Since the 40/70 mesh sand density is lighter than others, about half of injected particles are directly settled into the tank during the experiment. For the garnet, more particles deposit in the channel for the bed buildup. In Fig. 7(d), as the injection time increases, the particle bed gradually grows and narrows the flow gap, increasing the fluid friction. Therefore, the pressure has a positive relation with particle density. The maximum pressure, 16.97 kPa, is obtained at the final stage of the garnet injection. For 40/70 mesh sand, the pressure is the minimum of 16.63 kPa, and the bed takes 75 s to the equilibrium state.

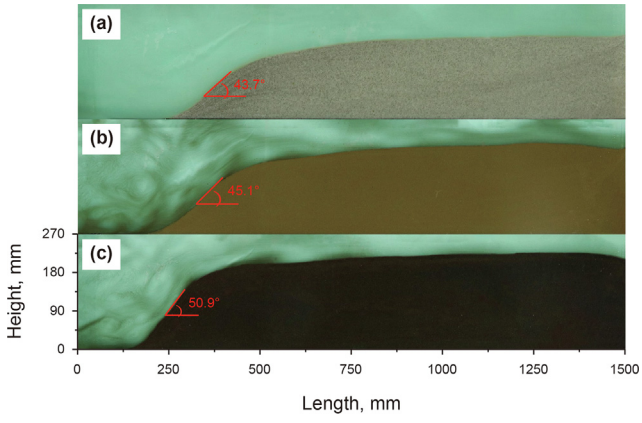

Fig. 6. The equilibrium states of 40/70 mesh particle beds at v_i = 0.42 m/s, μ_f = 0.001 Pa s, C_p = 4.2%, front view. (**a**) Sand; (**b**) Ceramsite; (**c**) Garnet.

3.2. Effect of fluid velocity

For hydraulic fracturing used in deep shale gas reservoirs, the fluid flow rate is usually large enough to ensure a high fluid velocity in fractures to enhance proppant transport (Isah et al., 2021). According to the liquid drag force equation exerted on a particle (Shook and Roco, 1992), particle transport in the narrow fracture significantly depends on the fluid velocity. Eq. (8) shows the relationship between fluid velocity and drag force.

$$F = \frac{0.5\pi}{4} C_D d^2 \rho_f v_i \tag{8}$$

where F is the drag force; C_d is the drag coefficient; d is the mean particle diameter. In the experiment, the mean fluid velocity in the channel are set to 0.17, 0.21, 0.42, and 0.50 m/s, the corresponding Re_f are 1008, 1246, 2492, and 2967. In Fig. 8, as the Re_f increases, the BEH significantly decreases because the high-speed fluid flow enhances the particle transport capacity. The BEH decreases from 89.2% to 52% for the 40/70 mesh sand bed at v_i = 0.5 m/s. Correspondingly, the BCA reduces from 79.8% to 30.1%. It indicates that more than half of the channel is not propped by particles. The value could increase as the denser particles are used. The linear fitting equations at three types of particles are suitable for the predictions of BEH and BCA, and R^2 values range from 0.95 to 0.98.

In Fig. 9, the dimensionless bed equilibrium heights (BEH) are quantitatively compared between our experimental results and the prediction data using Wang's model. The experimental results are more than the prediction values. For the denser particle of 40/70 mesh garnet, the maximum error is 16.0% at Re_f = 2492, and the average error is 12.5%. As the sand is used, the maximum error is 8.7% at Re_f = 1246, and the average error is 6.1%. The average value

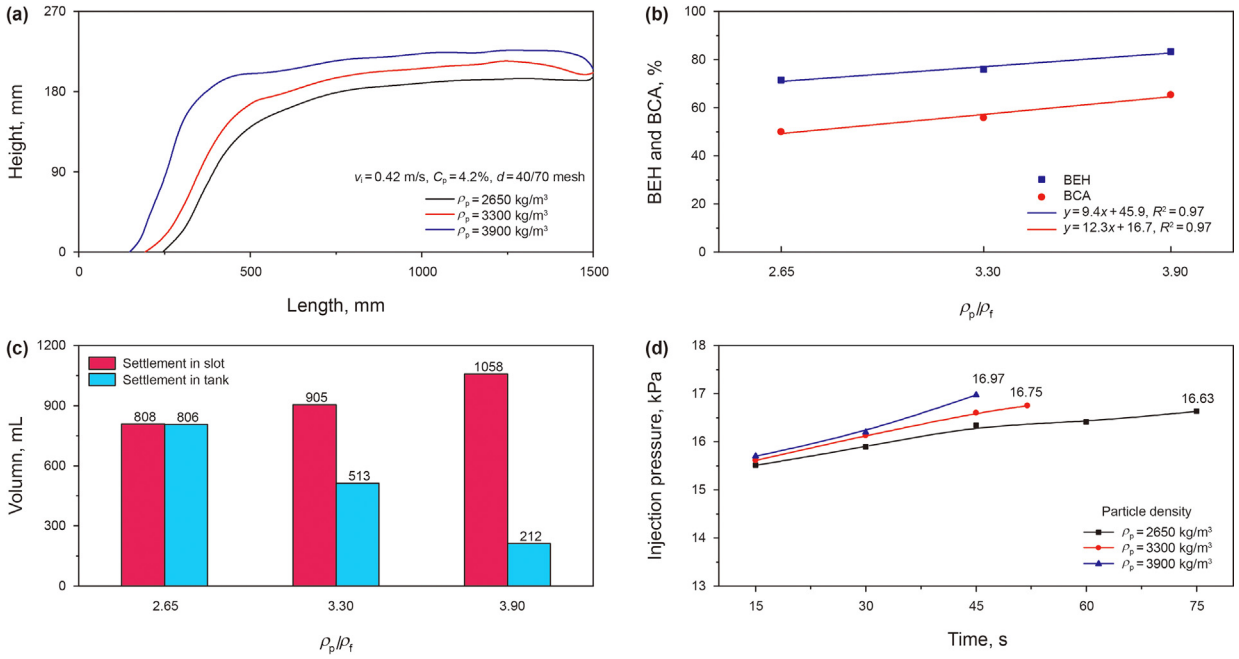

Fig. 7. The effect of particle densities on proppant distribution. (**a**) The bed profiles at equilibrium states; (**b**) The normalized equilibrium height and coverage area; (**c**) The particle volume in the channel and outlet tank; (**d**) Pressure data recorded by the pressure sensor at the entrance.

indicates that the heavy 40/70 mesh particle has more error than the light particle between the two models. According to our experiments, the 40/70 mesh particles could build up a particle bed higher than the value by the prediction model.

3.3. Effect of fluid viscosity

Slickwater with low viscosity is typically used in hydraulic fracturing in shale gas reservoirs because the fluid viscosity slows down the particle's settling velocity and extends their transport distance. In the experiment, the viscosity of fracturing fluid is set to 0.001, 0.003, 0.006, and 0.009 Pa s, respectively. The dimensionless parameter of Re_f represents the fluid viscosity. Based on Eq. (4), the Re_f decrease as the viscosity increases. From Fig. 10, it can be seen that the BEH and BCA have been significantly affected by the fluid viscosity. The BEH has a non-linear relationship with Re_f. Fitting a natural logarithmic law trend through experimental results yields a high coefficient of determination, R^2 ranges from 0.95 to 0.97. As the viscosity is more than 0.003 Pa s, the BEH sharply decreases. This indicates that particle suspension dominates the transport mechanism, and more injected particles cannot deposit in the channel. A similar fitting trend is found between the BCA and Re_f. The minimum value is only 18.1% for the 40/70 mesh sand.

It can infer that more particles prop the deep region of fractures if the high viscosity fluid is used, and the coverage area is minimal near the wellbore. This region would significantly lower the fracture conductivity. The decreasing pumping rate and pumping denser proppants are compensation measures.

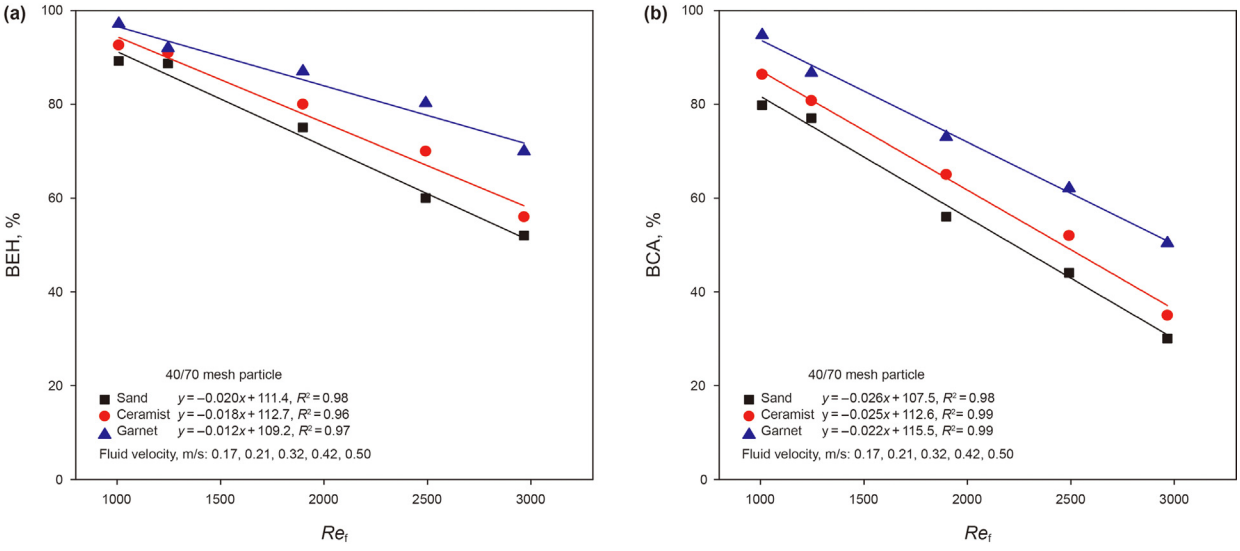

Fig. 8. The normalized bed size at μ_f = 0.001 Pa s, C_p = 1.0% with varied fluid velocities. (**a**) BEH; (**b**) BCA.

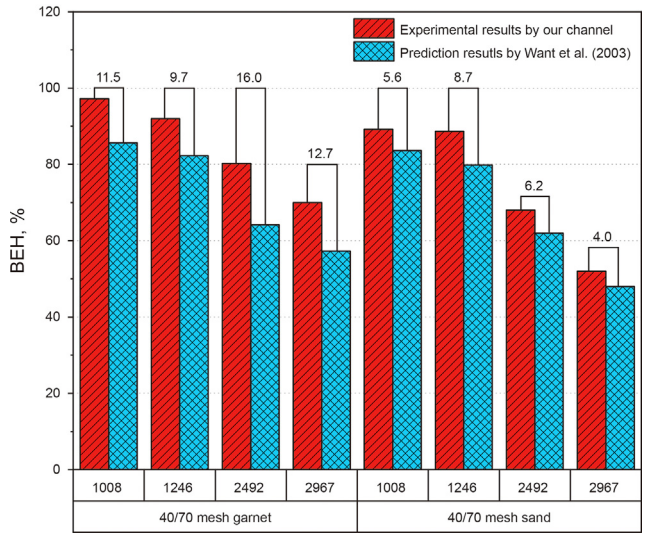

Fig. 9. Comparison of the dimensionless equilibrium height of 40/70 mesh particle bed between our experimental results and prediction data by Wang et al. (2003) at $\mu_f = 0.001$ Pa s, $C_p = 1.0\%$ with varied fluid velocities.

3.4. Effect of particle size

Since settlement velocity, drag force and lift force are all proportional to the square of the diameter in a Stroke's regime (Shook and Roco, 1992; Fjaestad and Tomac, 2019), particle transport in the fracture will be different from particles with different sizes. In Fig. 11, sand and garnet with 10/20, 20/40, 40/70, and 70/140 mesh are tested in the experiment, and the Shields number is used to represent the particle diameter. There is a natural logarithmic correlation between the Shields number and BEH, and R^2 ranges from 0.93 to 0.95. A similar trend is found between the BCA and *S*. When the minimum Shields number is 0.03 at 10/20 mesh garnet, the BEH and BCA are 80.0% and 59.0%. As the Shields number increases to 0.328 at 70/140 mesh sand, the BEH and BCA are 60.7% and 30.0%. According to the results, small particles tend to build up a lower bed further away from the inlet, which decreases the BCA.

3.5. Effect of particle volume fraction

The particle volume fraction in fracturing fluid plays a crucial role in the proppant placement in fractures. In Fig. 12, the volume fractions of three particle are set to 0.34%, 1.0%, 2.8%, and 4.2%, respectively. When the 40/70 mesh sand volume fraction is 0.34%, the BEH and BCA are 45.9% and 17.3%. With the increase of C_p, the BEH and BCA increase because more particles deposit in the channel. The possible reason is that frequent particle collisions at the high particle volume fraction lead to the loss of particle kinetic energy. The results demonstrate that the slurry with a low volume fraction leads to a fracture with low conductivity, which significantly affects production. For 40/70 mesh garnet, the BEH and BCA are 49.9% and 71.5% at $C_p = 4.2\%$. Both values increase to 65.3% and 83.3% as the garnet is used. Hence, the denser proppants can improve the value. The natural logarithmic law equations at three types of particles are suitable for the predictions of BEH and BCA, and R^2 values range from 0.94 to 0.99. A higher bed would be closer to the inlet at a large particle volume fraction, and the sand screenout is easily induced due to the poor particle motion.

3.6. Combination of multiple factors

The above experimental analysis shows that the independent variables have good correlations with the dependent values of BEH and BCA for nine types of particles, especially the 40/70 mesh particles. Multivariable linear regression is a suitable method for the best correlation between the dependent and independent variables. The linear regression models are obtained and expressed as

$$\mathrm{BEH} = -0.0009Re_f + 5\ln\left(\frac{C_p^{1.9}}{S^{3.1}}\right) + 5.9\frac{\rho_p}{\rho_f} + 18.5 \quad R^2 = 0.95 \tag{9}$$

$$\mathrm{BCA} = -0.005Re_f + 5\ln\left(\frac{C_p^{2.2}}{S^{3.5}}\right) + 7.9\frac{\rho_p}{\rho_f} - 0.85 \quad R^2 = 0.92 \tag{10}$$

BEH accuracy is evaluated by determining the percent error of

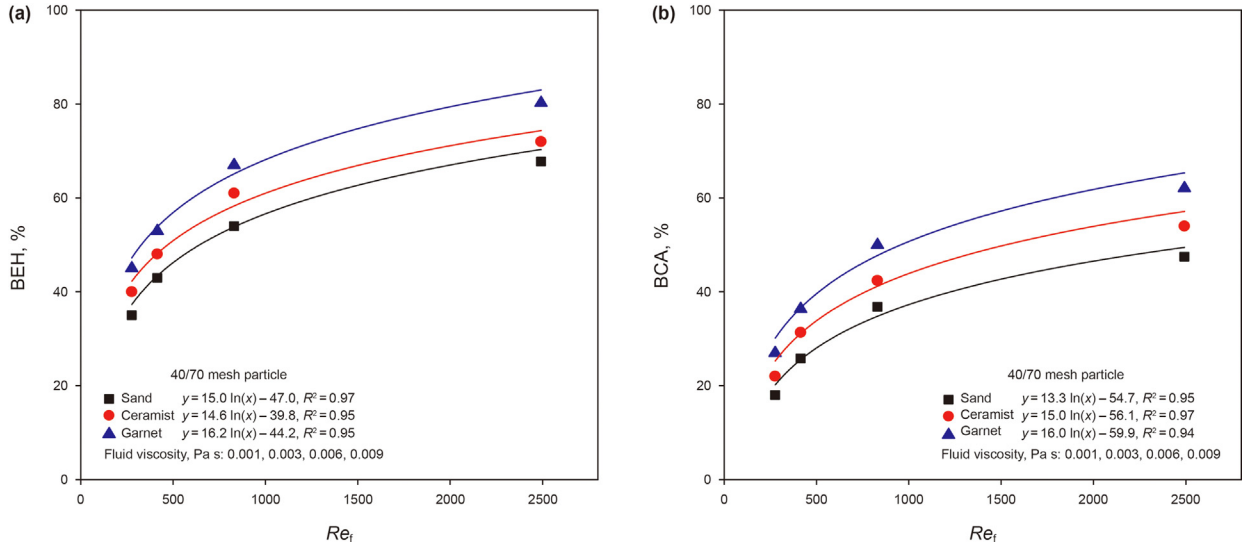

Fig. 10. The normalized bed size at $v_i = 0.42$ m/s, $C_p = 2.8\%$ with varied fluid viscosities. (**a**) BEH; (**b**) BCA.

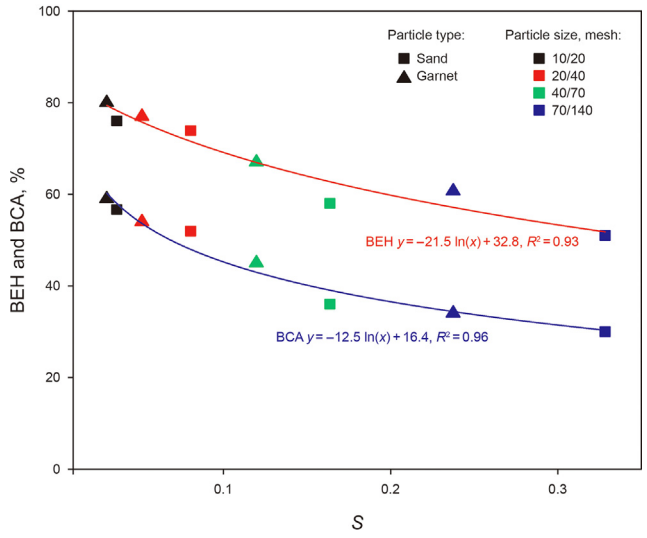

Fig. 11. The normalized bed size at $v_i = 0.42$ m/s, $\mu_f = 0.001$ Pa s, $C_p = 1.0\%$ with varied particle sizes.

the predicted BEH values relative to the measured BEH values by Eq. (11).

$$E_r = \left|\frac{BEH_{act} - BEH_{pre}}{BEH_{act}}\right| \times 100\% \quad (11)$$

where BEH_{act} is the measured value by the experiment; BEH_{pre} is the predicted value by the model.

The experimental data validate the accuracy of the regression model. Fig. 13(a) shows the predicted BEH values based on the training dataset and their calculated errors. The average error is 3.8%, and the maximum value is 10.9%. In Fig. 13(b), the average error is 6.8%, and the maximum value is 13.6%. The low errors indicate the high reliability of the models (Eqs. (9) and (10)) for predicting the equilibrium height and coverage area.

4. Discussion

4.1. The environmental pressure

In reality, a hydraulic fracture could initiate and propagate as the injected pressure at the entrance is more than the environmental pressure, equal to the sum of the formation confining pressure and friction pressure by fracture surfaces (Miskimins, 2020; Yew and Weng, 2014). For the typical experiment of particle transport, it is assumed that the slot with a constant width represents a propagating fracture, where the pressure has overcome the confining pressure (Sahai and Moghanloo, 2019). The primary reason is that it is a big challenge to exert confining pressure on transparent fracture surfaces. Due to the formation heterogeneity, the confining pressure is not a constant in the reservoir and significantly affects the injected pressure, leading to the violent fluctuation in the fracturing treatment (Singh et al., 2020). Hence, the varied pressure directly affects the fracture width based on the equation of fracture width (Miskimins, 2020). Since the slurry flow is very susceptible to the fracture width, the flow pattern and particle transport would significantly change within a fracture. As a result, the particle bed shape is probably different from our situation of the slot without confining pressure.

The experimental results tested by the planar slot are mainly used as the fundamental understanding for particle transport in a hydraulic fracture. The effect of environmental pressure on particle transport needs to be analyzed in future investigations.

4.2. The bed shape

The particle bed within a narrow fracture is in a dynamic equilibrium, and it is easily changed by the variation of the fluid and proppant properties during the test (Kern et al., 1959). According to the experimental results, it can conclude that the particle transport capacity directly affects the particle bed shape. The increases in fluid velocity and viscosity improve the carrying capacity of the fluid, which exerts enough force on particles to the deeper region. In addition, the apparent weight of a single particle is reduced by the decreases in particle density and size. The fluid could easily carry more particles in suspension, and a shorter bed would be built up in the slot. For the particle volume fraction, it is found that the

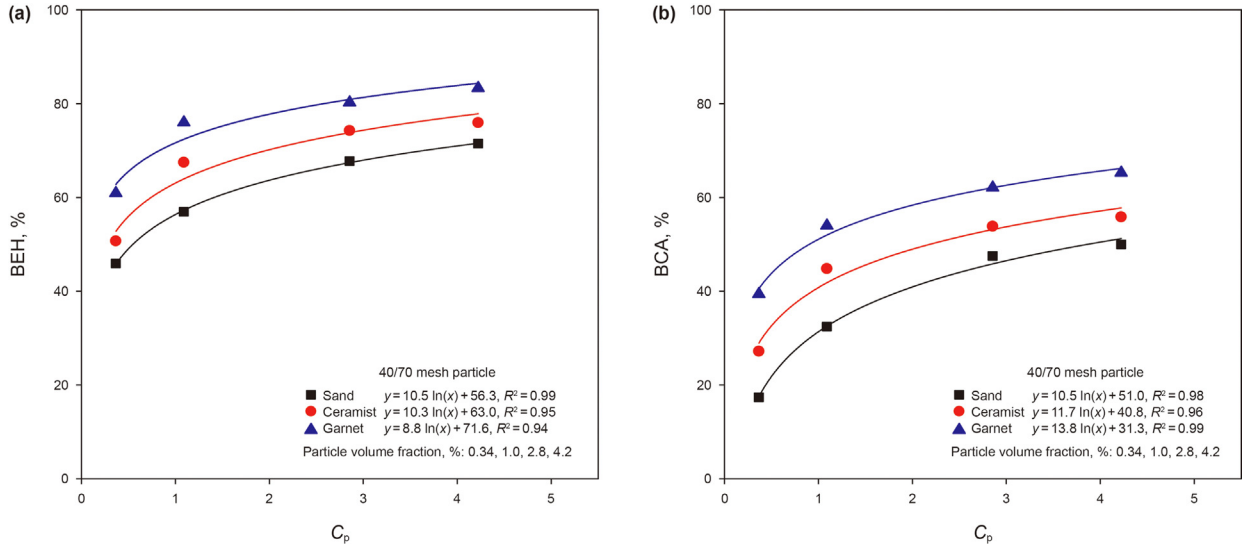

Fig. 12. The normalized bed size at $v_i = 0.42$ m/s, $\mu_f = 0.001$ Pa s with varied particle volume fractions. (**a**) BEH; (**b**) BCA.

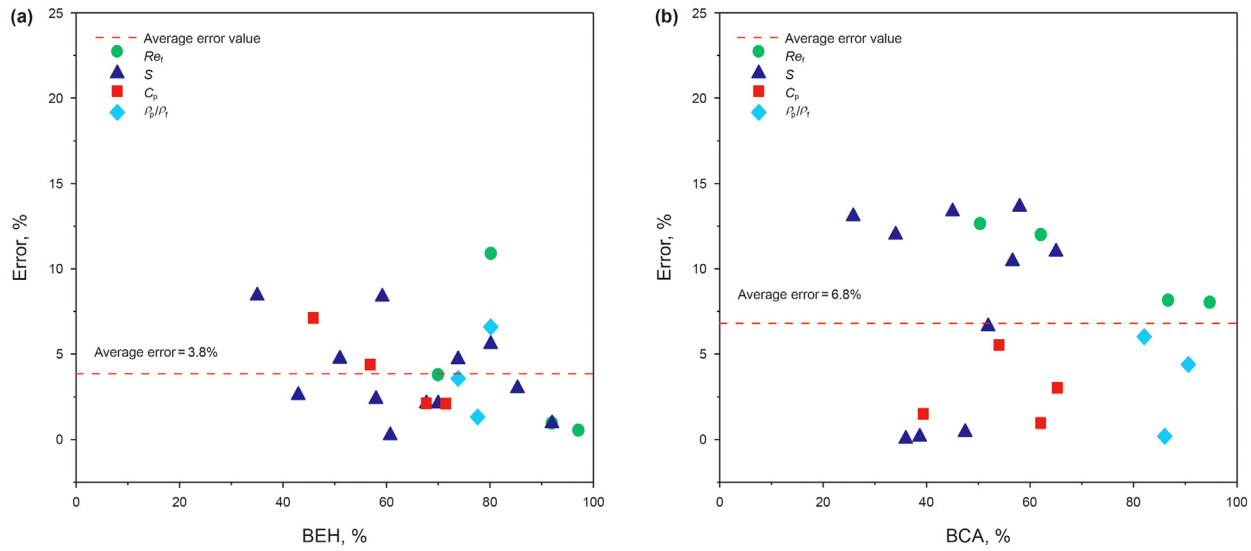

Fig. 13. (**a**) Error analysis of the predicted BEH values based on the training dataset; (**b**) Error analysis of the predicted BCA values based on the predicting dataset.

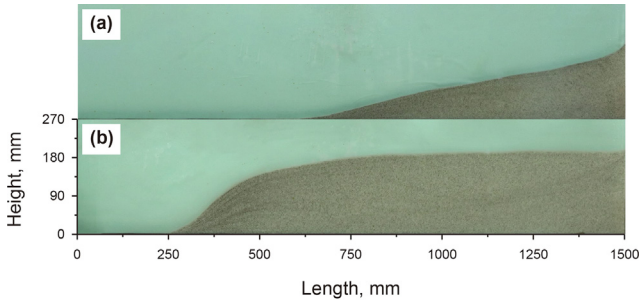

Fig. 14. The equilibrium states of 40/70 mesh sand beds at v_i = 0.42 m/s, μ_f = 0.001 Pa s, front view. (**a**) C_p = 0.34%; (**b**) C_p = 4.20%.

fluid can transport particles further into the slot, as shown in Fig. 14. The possible reason is a small number of collisions between particles. As a result, a sizeable depleted region is formed between the entrance and the front of the bed. Since many parameters have different effects on particle transport capacity, four dimensionless numbers are rational to represent the transport capacity of the slurry for analyzing the bed shape.

5. Conclusions

Small particle transport in a narrow fracture is a crucial factor affecting the fracture conductivity and stimulation effect in the deep shale reservoir. We first constructed a smooth narrow channel with a 3 mm width. Three types of particles with varied sizes are selected to test particle placement in the channel to improve the compatibility between the laboratory experiment and field application. Two key parameters, including the BEH and BCA, are obtained to investigate the effect of fluid velocity, fluid viscosity, particle density, particle size, and particle volume fraction on the proppant placement in a narrow fracture. Two correlation models are developed by the multiple linear regression method to predict the BEH and BCA of small particles in the narrow fracture. The following conclusion could be drawn from this study.

(1) In the narrow slot with a 3 mm width, 40/70 mesh particles are easily aggregated in the viscous fluid due to the limited flow space. Also, fluid fingers are formed near the inlet as the flow gap reduces. The aggregation can be avoided by using the low viscous fluid.
(2) The high-speed fluid velocity induces violent vortices near the inlet and disperses particles further into the channel. The deposited bed is far away from the inlet and leaves a depleted region without particles, significantly hindering the fluid flow from the reservoir. The region would increase at the low particle volume fraction.
(3) For 40/70 mesh particles, the experimental results of BEH in the narrower slot are more than the value predicted by the bi-power model developed by Wang et al. (2003) based on the large particles.
(4) Dimensionless parameters are rationally used to represent the transport capacity of the slurry for analyzing the BEH and BCA. There are linear laws and natural logarithmic laws between the dimensionless parameter and bed shape.
(5) The low errors indicate the high reliability of the developed correlation models for predicting the equilibrium height and coverage area as the small-size proppants are transported in the narrow fracture.

Acknowledgments

This work is supported by the Chongqing Research Program of Basic Research and Frontier Technology (Grants No. cstc2019jcyj-msxmX0006), Science and Technology Research Program of Chongqing Municipal Education Commission of China (Grant No. KJQN201801530 and KJQN201901511).

References

Ahmad, F.A., Miskimins, J.L., 2020. New experimental correlations to predict proppant distribution between perforation clusters using low viscosity fluids in a horizontal wellbore. In: SPE Annual Technical Conference and Exhibition. Society of Petroleum Engineers. https://doi.org/10.2118/201452-MS.
Alotaibi, M.A., Miskimins, J.L., 2018. Slickwater proppant transport in hydraulic fractures: new experimental findings and scalable correlation. SPE Prod. Oper. 33 (2), 164–178. https://doi.org/10.2118/174828-PA.
Ba Geri, M., Imqam, A., Dunn-Norman, S., 2018. Proppant transport behavior in inclined versus vertical hydraulic fractures: an experimental study. In: SPE/AAPG Eastern Regional Meeting. Society of Petroleum Engineers. https://

doi.org/10.2118/191813-18ERM-MS.
Babcock, R., Prokop, C., Kehle, R., 1967. Distribution of propping agent in vertical fractures. In: Drilling and Production Practice. API, New York, pp. 67–207.
Dominguez Ruben, L.G., Szupiany, R.N., Latosinski, F.G., López Weibel, C., Wood, M., Boldt, J., 2020. Acoustic Sediment Estimation Toolbox (ASET): a software package for calibrating and processing TRDI ADCP data to compute suspended-sediment transport in sandy rivers. Comput. Geosci. 140, 104499. https://doi.org/10.1016/j.cageo.2020.104499.
Fernández, M.E., Sánchez, M., Pugnaloni, L.A., 2019. Proppant transport in a scaled vertical planar fracture: vorticity and dune placement. J. Petrol. Sci. Eng. 173, 1382–1389. https://doi.org/10.1016/j.petrol.2018.10.007.
Fjaestad, D., Tomac, I., 2019. Experimental investigation of sand proppant particles flow and transport regimes through narrow slots. Powder Technol. 343, 495–511. https://doi.org/10.1016/j.powtec.2018.11.004.
Isah, A., Hiba, M., Al-Azani, K., Aljawad, M.S., Mahmoud, M., 2021. A comprehensive review of proppant transport in fractured reservoirs: experimental, numerical, and field aspects. J. Nat. Gas Sci. Eng. 88, 103832. https://doi.org/10.1016/j.jngse.2021.103832.
Kern, L., Perkins, T., Wyant, R., 1959. The mechanics of sand movement in fracturing. J. Petrol. Technol. 11 (7), 55–57. https://doi.org/10.2118/1108-g.
Li, P., Zhang, X., Lu, X., 2018. Numerical simulation on solid-liquid two-phase flow in cross fractures. Chem. Eng. Sci. 181, 1–18. https://doi.org/10.1016/j.ces.2018.02.001.
Li, X., Li, M., Amoudry, L.O., Ramirez-Mendoza, R., Thorne, P.D., Song, Q., Zheng, P., Simmons, S.M., Jordan, L.-B., McLelland, S.J., 2020. Three-dimensional modelling of suspended sediment transport in the far wake of tidal stream turbines. Renew. Energy 151, 956–965. https://doi.org/10.1016/j.renene.2019.11.096.
Liu, Y., 2006. Settling and Hydrodynamic Retardation of Proppants in Hydraulic Fractures. Ph.D. Dissertation. The University of Texas at Austin. https://doi.org/10.1201/b16287-17.
Liu, Y., Sharma, M.M., 2005. Effect of fracture width and fluid rheology on proppant settling and retardation: an experimental study. In: SPE Annual Technical Conference and Exhibition. Society of Petroleum Engineers. https://doi.org/10.2118/96208-MS.
Mack, M., Sun, J., Khadilkar, C., 2014. Quantifying proppant transport in thin fluids: theory and experiments. In: SPE Hydraulic Fracturing Technology Conference. Society of Petroleum Engineers. https://doi.org/10.2118/168637-MS.
McClure, M., 2018. Bed load proppant transport during slickwater hydraulic fracturing: insights from comparisons between published laboratory data and correlations for sediment and pipeline slurry transport. J. Petrol. Sci. Eng. 161, 599–610. https://doi.org/10.1016/j.petrol.2017.11.043.
Miller, M.C., McCave, I.N., Komar, P.D., 1977. Threshold of sediment motion under unidirectional currents. Sedimentology 24 (4), 507–527. https://doi.org/10.1111/j.1365-3091.1977.tb00136.x.
Miskimins, J., 2020. Hydraulic Fracturing: Fundamentals and Advancements. Society of Petroleum Engineers.
Novotny, E.J., 1977. Proppant transport. In: SPE Annual Fall Technical Conference and Exhibition. Society of Petroleum Engineers. https://doi.org/10.2118/6813-MS.
Patankar, N.A., Joseph, D., Wang, J., Barree, R., Conway, M., Asadi, M., 2002. Power law correlations for sediment transport in pressure driven channel flows. Int. J. Multiphas. Flow 28 (8), 1269–1292. https://doi.org/10.1016/s0301-9322(02)00152-0.
Qu, H., Hu, Y., Liu, Y., Wang, R., Tang, S., Xue, L., 2021a. The study of particle-fluid flow in narrow, curved slots to enhance comprehension of particle transport mechanisms in complex fractures. J. Nat. Gas Sci. Eng. 92, 103981. https://doi.org/10.1016/j.jngse.2021.103981.
Qu, H., Tang, S., Liu, Z., McLennan, J., Wang, R., 2021b. Experimental investigation of proppant particles transport in a tortuous fracture. Powder Technol. 382, 95–106. https://doi.org/10.1016/j.powtec.2020.12.060.
Qu, H., Wu, X., Liu, Y., Feng, Y., Tang, S., Zhang, S., Hu, Y., 2020. Effect of shale mineralogy characteristics on the perforation performance and particle fragmentation of abrasive waterjet. Powder Technol. 367, 427–442. https://doi.org/10.1016/j.powtec.2020.03.068.
Ren, J., Zhao, M., Zhang, W., Xu, Q., Yuan, J., Dong, B., 2020. Impact of the construction of cascade reservoirs on suspended sediment peak transport variation during flood events in the Three Gorges Reservoir. Catena 188, 104409. https://doi.org/10.1016/j.catena.2019.104409.
Sahai, R., Miskimins, J.L., Olson, K.E., 2014. Laboratory results of proppant transport in complex fracture systems. In: SPE Hydraulic Fracturing Technology Conference. Society of Petroleum Engineers. https://doi.org/10.2118/168579-MS.
Sahai, R., Moghanloo, R.G., 2019. Proppant transport in complex fracture networks – a review. J. Petrol. Sci. Eng. 182, 106199. https://doi.org/10.1016/j.petrol.2019.106199.
Schols, R.S., Visser, W., 1974. Proppant bank buildup in a vertical fracture without fluid loss. In: SPE European Spring Meeting. Society of Petroleum Engineers. https://doi.org/10.2118/4834-MS.
Shook, C.A., Roco, M.C.R., 1992. Slurry Flow: Principles and Practice. Butterworth-Heinemann, New York. https://doi.org/10.1016/0032-5910(92)87015-3, 1992.
Singh, A., Liu, X., Jiehao, W., Rijken, P., Stribling, M., Wildt, P., Anschutz, D., 2020. New comprehensive large tortuous slot flow testing for unconventional fracturing. In: SPE Annual Technical Conference and Exhibition. Society of Petroleum Engineers. https://doi.org/10.2118/201578-ms.
Tong, S., Mohanty, K.K., 2016. Proppant transport study in fractures with intersections. Fuel 181, 463–477. https://doi.org/10.1016/j.fuel.2016.04.144.
Wang, J., Joseph, D.D., Patankar, N.A., Conway, M., Barree, R.D., 2003. Bi-power law correlations for sediment transport in pressure driven channel flows. Int. J. Multiphas. Flow 29 (3), 475–494. https://doi.org/10.1016/s0301-9322(02)00152-0.
Woodworth, T.R., Miskimins, J.L., 2007. Extrapolation of laboratory proppant placement behavior to the field in slickwater fracturing applications. In: SPE Hydraulic Fracturing Technology Conference. Society of Petroleum Engineers. https://doi.org/10.2118/106089-MS.
Yew, C.H., Weng, X., 2014. Mechanics of Hydraulic Fracturing, 2nd ed. Gulf Professional Publishing.
Zeng, J., Li, H., Zhang, D., 2019. Numerical simulation of proppant transport in propagating fractures with the multi-phase particle-in-cell method. Fuel 245, 316–335. https://doi.org/10.1016/j.fuel.2019.02.056.
Zhang, G., Gutierrez, M., Li, M., 2017. A coupled CFD-DEM approach to model particle-fluid mixture transport between two parallel plates to improve understanding of proppant micromechanics in hydraulic fractures. Powder Technol. 308, 235–248. https://doi.org/10.1016/j.powtec.2016.11.055.
Zheng, W., Silva, S.C., Tannant, D.D., 2018. Crushing characteristics of four different proppants and implications for fracture conductivity. J. Nat. Gas Sci. Eng. 53, 125–138. https://doi.org/10.1016/j.jngse.2018.02.028.
Zohuri, B., 2017. Dimensional Analysis beyond the Pi Theorem. Dimensional Analysis Beyond the Pi Theorem. https://doi.org/10.1007/978-3-319-45726-0.